IEEE Photonics Journal
An IEEE Photonics Society Publication

Open Access

Spectrally Resolved Single-Photon Timing of Silicon Photomultipliers for Time-Domain Diffuse Spectroscopy

Volume 7, Number 4, August 2015

E. Martinenghi
A. Dalla Mora
D. Contini
A. Farina
F. Villa, Member, IEEE
A. Torricelli
A. Pifferi

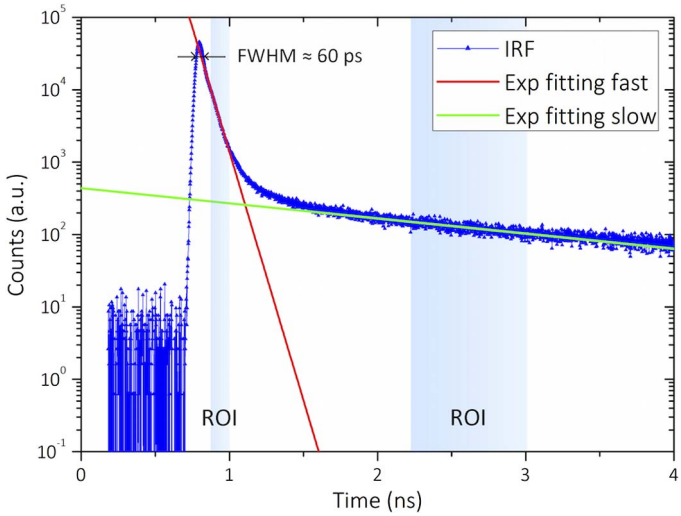

DOI: 10.1109/JPHOT.2015.2456070
1943-0655

IEEE photonics SOCIETY

IEEE

Spectrally Resolved Single-Photon Timing of Silicon Photomultipliers for Time-Domain Diffuse Spectroscopy

E. Martinenghi,[1] A. Dalla Mora,[1] D. Contini,[1] A. Farina,[2] F. Villa,[3] *Member, IEEE*, A. Torricelli,[1] and A. Pifferi[1,2]

[1]Dipartimento di Fisica, Politecnico di Milano, 20133 Milano, Italy
[2]Istituto di Fotonica e Nanotecnologie, Consiglio Nazionale delle Ricerche, 20133 Milano, Italy
[3]Dipartimento di Elettronica, Informazione e Bioingegneria, Politecnico di Milano, 20133 Milano, Italy

DOI: 10.1109/JPHOT.2015.2456070

Manuscript received June 12, 2015; revised July 10, 2015; accepted July 11, 2015. Date of publication July 15, 2015; date of current version July 30, 2015. This work was supported by the European Community's Seventh Framework Program under Grant Agreement LASERLAB EUROPE no. 284464.
E. Martinenghi and A. Dalla Mora contributed equally to this work. Corresponding author: A. Farina (e-mail: andrea.farina@ifn.cnr.it).

Abstract: We characterized the single-photon timing response function of various silicon photomultipliers (SiPMs) over a broad (500–1100 nm) spectral range. We selected two SiPM manufacturers, and we investigated two active areas, i.e., a small (1–1.69 mm^2) and a large (9 mm^2) one, for each of them. We demonstrate that selected SiPMs are suitable for time-resolved diffuse optics (DO) applications where a very large detection area and sensitivity down to single photons are crucial to detecting the very faint return signal from biological tissues, like the brain, thus allowing replacement of photomultiplier tubes and opening the way to a novel generation of DO multichannel instrumentation. Due to our custom front-end electronics, we show the world's best single-photon timing resolution for SiPMs, namely, 57-ps full-width at half maximum for Hamamatsu 1.69 mm^2 and 115 ps for Excelitas 9 mm^2. Even further, we provide a thorough spectral investigation of the full single-photon timing response function, also detailing diffusion tails' time constants and dynamic range. The achieved insight and the reported performance open the way to a widespread diffusion of SiPMs not just in many-photon regimes (e.g., PET) but at single-photon counting regimes like DO as well.

Index Terms: Photodetectors, single-photon detectors, photon counting, photon timing, silicon photomultiplier (SiPM), timing resolution.

1. Introduction

Silicon photomultipliers (SiPMs) are recently spreading over the wide single-photon detectors scenario, thanks to many advantages compared to traditional Photomultiplier Tubes (PMTs), such as low cost, ruggedness, compactness, insensitivity to electromagnetic fields, Complementary Metal-Oxide Semiconductor (CMOS) process compatibility, and related possibility of customization [1], [2]. Nowadays, SiPM's driving applications are related to the detection of scintillation light, such as in Positron Emission Tomography (PET) systems, where hundreds of SiPMs are parallelized in dense structures to cover wide detection areas and where bunches of thousands of scintillation photons hit each SiPM a time [3]. Instead, until now the employment of SiPM in single-photon applications has been limited mainly due to high noise and poor timing resolution. Only very recently,

SiPMs have been proposed as a possible alternative detector also in the field of Time-Resolved (TR) Diffuse Optics (DO) [4], [5], mainly thanks to the possibility of having large active area (crucial for enhancing the photon harvesting from diffusive medium) and single-photon sensitivity. In fact, in a preliminary characterization, we recently successfully explored the use of SiPMs for time-resolved measurements on photon diffusive samples [6].

Nowadays TR-DO systems are mostly based on traditional bulky, expensive and fragile PMTs [7], which severely impact on the overall system complexity, cost, and dimension, thus impairing their wide diffusion. Since TR-DO systems rely on the precise measurement of the single-photon arrival time, a sharp photon timing response is of the utmost importance. Furthermore, many DO applications employ pulsed laser excitation at different wavelengths, like in functional Near-InfraRed Spectroscopy (fNIRS) [7], [8], optical mammography [9], quality assessment of food [10], wood [11], pharmaceuticals [12]), etc. For that reason, the detector must provide high performance over a wide wavelength spectrum. SiPMs bring a number of advantages such as wide active area (up to few square millimeters) and numerical aperture (both directly reflect into high photon collection efficiency), high quantum efficiency (easily exceeding 20% at 600 nm wavelength), broad spectral coverage (350–1100 nm), and the typical compactness of solid-state devices. SiPMs are also very cheap (much less than 100 $ for a single device) and require neither bulky instrumentation for biasing and operation, nor complex electronics for detection sensing; they are also insensitive to electromagnetic fields and to strong light exposure. Even further, the possibility of replacing PMTs with solid-state SiPMs enables novel scenarios, since the number of measuring channels of TR-DO systems can be drastically increased, easily reaching values (e.g., 128 channels) that are practically unfeasible with present technology but that have a key role in many applications, like in fNIRS for obtaining high-resolution maps of the brain activity.

Basically, a SiPM is an array of microcells, each one consisting of a Single-Photon Avalanche-Diode (SPAD) together with an integrated quenching resistor for avalanche passive quenching and self-reset. The microcells are connected in parallel all together, to form a two terminal detector, with one global anode and one global cathode. The overall SiPM performance strongly depends on microcells cross-section and lattice quality, on the overall number of microcells, device dimensions, parameters uniformity, stray capacitances and metal lines routing.

In TR-DO, the Instrument Response Function (IRF) is defined by the response of the instrument to a sharp laser pulse. Typically, it is given by the convolution of laser pulse shape, the detector response function and other time-jitter contributions from the electronic detection chain. The typical SiPM response is characterized by a Gaussian peak, which can be quantified through the Full-Width at Half-Maximum (FWHM), also called Single-Photon Time Resolution (SPTR), and an exponential decaying tail: the so-called “diffusion tail” that can be quantified by the exponential time constant. This contribution results fundamental since it can hide trailing signal photons and affects a number of Diffuse Optics measurements [13], thus even preventing tomographical reconstructions [14] or topographical images of deep inclusions inside diffusive media [15].

In this work, we particularly focus on the characterization of the response shape of both small (1–1.69 mm^2) and large (9 mm^2) active area SiPMs, over a broad spectral range from 500 nm to 1100 nm. The targeted devices are produced by two different manufacturers, namely Hamamatsu Photonics (Japan) and Excelitas Technologies (Canada). In the followings, we first describe the important contributions to the IRF then the experimental setup employed for the characterization, and finally we discuss the obtained results. The first parameter we report is the SPTR, for which we achieved the best performance ever reported in literature (to the best of our knowledge), that is 57 ps for a small SiPM and 115 ps for a large one. Then, we focus on the “diffusion tail,” by reporting both the exponential decay time constants and the resulting dynamic range of the IRF curve. In the end, we report the SiPM noise behavior versus temperature.

2. Instrument Response Function

Fig. 1 shows a typical IRF plot that we measured in the SiPM under test, from which it results evident the presence of the constant background noise, the Gaussian peak, and two

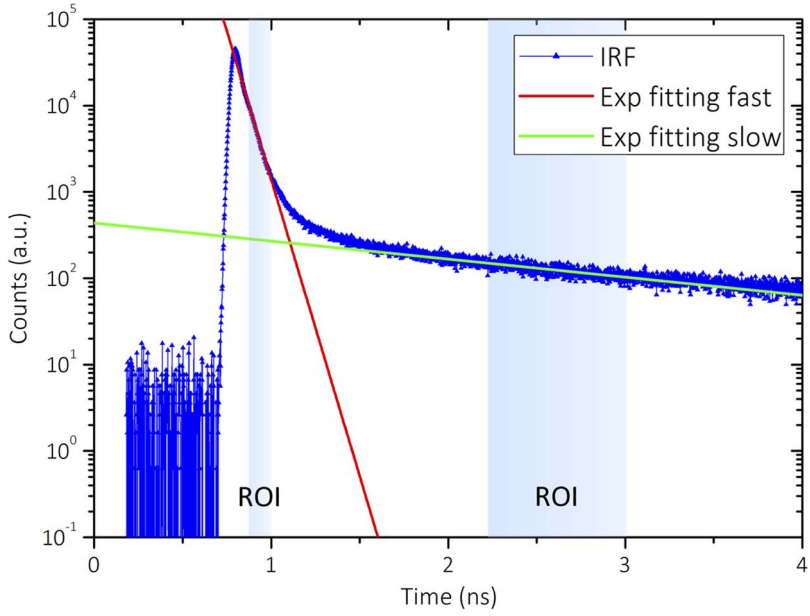

Fig. 1. Typical Instrument Response Function (IRF), with two highlighted Regions Of Interest (ROI), where the exponential fitting for computing the time constants of the slow and fast decays is applied.

exponential decaying tails. The leading noise is due to both primary carrier generation (e.g., Shockley-Read-Hall mechanism, direct band-to-band tunneling and trap-assisted tunneling [16]) and to secondary ignitions due to afterpulsing [17] and crosstalk. In order to quantitatively assess the global IRF shape we identified two different Regions Of Interest (ROI) at a given time delay from the main IRF peak, where it is possible to exponentially fit the response decay with a single time constant for each ROI, as shown Fig. 1. Then we computed the Dynamic Range (DR) of the IRF curve, which is defined as the ratio between the IRF peak and the residual tail intensity after a defined time delay from the peak. We decided to select a 1.5 ns delay, since it is often considered a reference value for "late" photons in many DO measurements [18].

The SPTR component of the IRF is the total Gaussian jitter σ^2_{TOT}, which given by many contributions:

$$\sigma^2_{TOT} = \sigma^2_{int} + \sigma^2_{tt} + \sigma^2_{mis} + \sigma^2_{noise} + \sigma^2_{setup} \quad (1)$$

where σ^2_{int} is the SiPM microcell intrinsic jitter, σ^2_{tt} is the spread in electrical transit time among microcells close to and far from the anode/cathode pads, σ^2_{mis} is the mismatch among microcells due to process tolerances, σ^2_{noise} is the time-jitter due to the noise of the detector and the electronics, and σ^2_{setup} is the time-jitter of the remaining setup components (i.e., laser, timing electronics, etc.). The intrinsic time jitter is due to the avalanche build up, the photon absorption position within the depleted region, and the statistics of the avalanche lateral propagation over the microcell active area [19]. For each microcell, the intrinsic jitter depends on photon wavelength and improves by increasing the excess bias V_{EX} (i.e., the operating voltage above breakdown). Usually the intrinsic jitter is lower than 30 ps FWHM, hence it is often negligible in SiPMs showing total FWHM typically broader than 100 ps. The transit time spread and microcell mismatches strongly depend on SiPM layout (and bonding pad routing) and in large SiPMs it can result in more than 100 ps between the inner and the outermost microcell [20].

At the end, the voltage noise of detector, σ^2_{DCR}, and electronics, σ^2_{ele}, are often the dominant contribution in the overall SPTR [20]. When using the leading-edge discriminator technique for time stamping the avalanche ignition, both SiPM Dark Count Rate (DCR) and electronics noise

directly impact the timing resolution, since they cause fluctuations of the SiPM output signal base-line [21]. Such a time jitter is inversely proportional to the slope dV/dT of the avalanche leading-edge at the threshold crossing, as given by

$$\sigma^2_{\text{noise}} = \frac{\sigma^2_{\text{DCR}} + \sigma^2_{\text{ele}}}{\frac{dV}{dT}}. \tag{2}$$

This contribution depends on the excess bias value and since both the leading-edge slope and DCR increase with V_{EX} there is an optimum bias voltage that minimizes the SPTR. The detrimental effect of DCR on timing resolution can be mitigated by shrinking the time duration of the single microcell response, by means of an appropriate filtering or by using a smarter discrimination technique, such as the Constant Fraction Discriminator (CFD) [22]. Eventually, the setup jitter can be easily measured (e.g., by saturating the SiPM with an intense light pulse) and then subtracted from the total jitter.

To the best of our knowledge, the best results so far achieved in terms of SPTR are 75 ps and 180 ps, for a 1 mm^2 and for a 9 mm^2 area device, respectively [20], [23]. However there are very few works focused on the SiPM characterization at the single-photon level [24], [25], since most authors discuss only the Coincidence Time Response (CTR) of SiPM, when excited by the very many photons, coming out from a scintillator.

Apart from the SPTR, the overall SiPM IRF shape and in particular the presence of exponentially decaying tails and their origin is not much discussed in literature. Ref. [24] suggests that the presence in the IRF of delayed photons can be due to the detector afterpulsing. However this hypothesis is not consistent with the measurement technique employed, in which only the arrival time of the first photon per laser pulse is acquired, thus avoiding the detection of secondary after-pulse ignitions. For the same reason, also (electrical and optical) crosstalks cannot be the cause of the IRF tail. Instead, the presence of an exponential tail in the IRF of SPADs is well known in literature and it is mainly attributed to photons absorbed in the neutral region of the semiconductor, beyond the depleted space-charge region, where there is no electric field. Indeed, in a solid-state single-photon detector, carriers photogenerated within those neutral regions do not quickly drift (since there is no electric field), but they slowly diffuse (almost randomly), and eventually can succeed in reaching the depleted region being swiftly accelerated by the electric field therein, and possibly triggering an avalanche process, very much delayed (even nanoseconds) in respect to the photon arrival time. For this reason, the IRF exponential decay is often called “diffusion tail” [26]. The time constant of such a tail can be computed as [27]

$$\tau_{\text{tail}} = \frac{W^2}{\pi^2 D_n} \tag{3}$$

where W is the neutral region thickness, and D_n is the minority carriers diffusion coefficient (about 36 cm^2/s and 12 cm^2/s for electrons and holes, respectively, in silicon). The same phenomenon explains the presence of a tail also in the IRF of SiPMs. In SPAD detectors, this tail can be suppressed by introducing a buried junction (e.g., a n-p one under the p-on-n shallow junction, or vice versa a p-n one under the n-on-p shallow one) to sweep away the carrier that could trigger the ignition, for example, by means of a deep “buried layer” as in [28], or a very highly doped substrate (e.g. a n+ substrate under the p-on-n main shallow junction, or vice versa a p+ substrate under the n-on-p junction). Hence, the same solutions can be implemented also in SiPM design in order to suppress the long tail, thus improving the dynamic range by orders of magnitude.

In SPAD detectors, the DCR affects the IRF tail, as discussed by [29]: if an avalanche is ignited when the SPAD is not completely recovered after a previous dark count, the output signal amplitude results lower (due to the lower effective excess bias), hence triggering the timing electronics with a time delay. In SiPMs, only pileup within a microcell (a very rare event) results

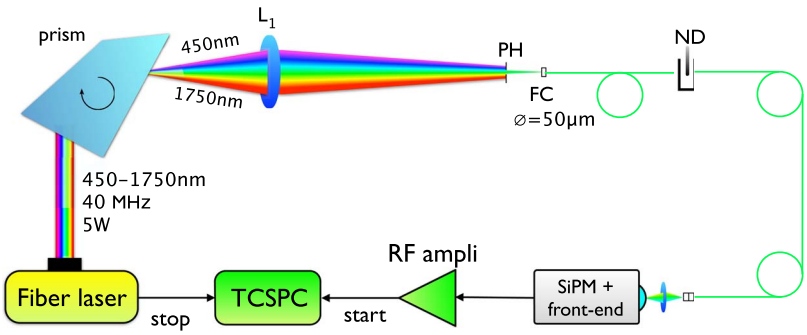

Fig. 2. Experimental setup. L1—lens; PH—pinhole; FC—fiber core; ND—neutral density filter; RF ampli—radiofrequency amplifier.

in a similar effect, whereas pileup in different microcells causes an increased output signal amplitude, thus threshold crossing ahead of time, which is the opposite of an IRF tail. Nevertheless, in Section 3.2, when describing the SiPM front-end, we show also how DCR can originate an IRF tail in setups like ours.

3. Experimental Set-Up

For the characterization of the SiPMs response we employed a broadband Time-Correlated Single-Photon Counting (TCSPC) system [30], as shown in Fig. 2. A supercontinuum laser source (NKT Photonics, Denmark) provides a total output power of about 5 W over a broad spectrum, spreading from 450 nm to 1750 nm. By means of a prism, the white light pulse was first separated into different wavelengths, with a spectral resolution narrower than 10 nm, and then launched into a 50 μm core optical fiber, through a focusing lens. A pinhole was inserted before the fiber head to avoid back-reflections to the laser. The prism incidence angle was set by a software controlled stepper motor: each motor step was associated to a single wavelength coupled into the fiber, after proper calibration with a commercial spectrometer. A Neutral Density (ND) variable attenuator allows to adjust the proper optical power down to the single-photon level onto the SiPM active area. Another lens was used to provide a collimated light onto the SiPM active area, in order to uniformly excite the entire area.

3.1. Pulsed Laser

The laser repetition rate was set to 40 MHz; the time width of the laser pulse was lower than 10 ps FWHM for most of the wavelengths over the whole 500 nm–1100 nm spectral range. In fact, by using a commercial SPAD module (PDM50, MPD, Italy) with 35 ps FWHM timing resolution over the entire spectral range, we proved that the laser pulse width increases at wavelengths shorter than 600 nm, and the laser pulse width becomes 100 ps at 550 nm and 150 ps at 500 nm, as well as 65 ps at 1065 nm (here, the worsening is probably due to spurious light from the 1064 nm laser pump).

3.2. Front-End Electronics

Concerning the electronics, we optimized the front-end circuit we reported in [6], tailored to extract the best timing performance out of the SiPM. As explained in Section 2, DCR and electronic noise limit the SiPM timing performance since they cause fluctuations in the output signal base-line. For this reason we conceived the front-end circuitry aiming at reducing such fluctuations. The SiPM is AC coupled to an amplifier through a capacitor, which performs a high-pass filtering of the avalanche onset, thus significantly shrinking the time duration of the single microcell response and consequently reducing the pile-up probability. The wide-bandwidth and low-noise amplifier is a VT120 by Ortec (USA), specifically designed for PMTs and silicon detectors. Our front-end circuit benefits from its less than 20 μV rms equivalent input noise, for minimizing

the base-line fluctuation, and the wide 350 MHz bandwidth, for maximizing the output signal leading-edge slope. The amplifier output feeds the "start" trigger to the TCSPC board (SPC130, Becker & Hickl GmbH, Germany); instead the "stop" trigger is provided by an electric synchronism, internally generated by the laser. The timing board accurately marks the photon arrival time thanks to the presence of an input CFD (see discussion in Section 2), thus further reducing time jitter caused by variation of signal amplitude. Eventually, the TCSPC board reconstructs the histogram of the arrival times of the single-photons hitting the SiPM under test.

The AC-coupling, which has clear advantages in terms of SPTR, could be the cause of the fast IRF tail shown in Fig. 1. In fact the output signal has a very fast and intense positive peak (given by the derivative of the microcell avalanche fast rising-edge), followed by a negative overshoot, of hundreds of picosecond duration (due to the derivative of the microcell recovery to quiescence). If a signal photon piles-up during the negative overshoot originated by a previous dark count, it would trigger a delayed "start" signal and, hence, a "tail" in the IRF. This phenomenon justifies a tail with a time constant of less than hundred picoseconds, compatible with the "fast" decay of Fig. 1.

3.3. Devices Under Test

In this paper, we characterized SiPMs produced by two manufacturers, Hamamatsu Photonics and Excelitas Technology. Both devices have a p-on-n structure (i.e., a shallow p+ diffusion into an n epitaxial layer), thus electrons are the main responsible to avalanche ignitions at short wavelength (i.e., when photons are absorbed within the p+ shallow diffusion) while holes are mainly responsible to avalanche ignitions at long wavelength (i.e., when photons are absorbed in the deep n layer). Since in silicon electrons have a much higher impact ionization efficiency than holes, these p-on-n SiPMs have a Photon Detection Efficiency (PDE) optimized for the Near Ultraviolet (NUV). Vice versa, n on p SiPMs are sometimes referred to as Red-Greed-Blue (RBG) SiPMs, given the better response in the visible wavelength range.

In SPADs, junction structure and device cross-section (either p-on-n or n-on-p) slightly impact timing resolution, while they have almost no influence in SiPMs, since the SPTR is not dominated by the microcell intrinsic jitter. Nevertheless, the SiPM structure affects the diffusion tail caused by photons absorbed in the neutral region. As we have shown in (3), the tail time constant is inversely proportional to the diffusion coefficient of the minority carriers involved in the avalanche ignition: since this coefficient is lower for holes (about 12 cm^2/s in silicon) than for electrons (about 36 cm^2/s in silicon), p-on-n structures reveal a longer diffusion tail. Unfortunately, the cross-section of the SiPM under test is kept confidential by the manufacturers, so no quantitative info is available about their structure. Nevertheless, considering a reasonable neutral region thickness of 5 μm and the given p-on-n structure, the resulting time constant is about $\tau = 2$ ns, compatible with the slower tail shown in the results section, as discussed in the followings.

Since the DCR has a strong impact on the IRF we selected devices with low noise, by Hamamatsu and Excelitas, with the performance given in Table 1. In particular we selected Excelitas SiPMs with 100 kcps and 500 kcps DCR at room temperature, respectively for small and large area devices, and Hamamatsu SiPMs with 50 kcps and 300 kcps at room temperature, respectively, for small and large area devices. The slightly higher DCR of Excelitas devices is counterbalanced by a lower terminal capacitance (20 pF and 175 pF for Excelitas SiPMs compared to 60 pF and 320 pF for Hamamatsu ones), which determines faster output signal slope and, hence, better timing resolution.

4. Measurements

Each SiPM detector was preliminary characterized with a parameter analyzer, in order to measure its breakdown voltage and to choose the proper biasing point at which SPTR and background noise result optimal. For each detector, the IRF was acquired at different wavelengths, starting from 500 nm up to 1100 nm, with 10 nm steps, at room temperature. Since the TCSPC

TABLE 1

Features of the tested SiPM devices

	Hamamatsu 1.3 mm x 1.3 mm [S13081-050CS]	**Hamamatsu 3 mm x 3 mm** [S13082-4084]	**Excelitas 1 mm x 1 mm** [C3074011050C]	**Excelitas 3 mm x 3 mm** [C3074233050C]
Name in this work	HAM-13	HAM-30	EXC-10	EXC-30
Total active area	1.69 mm^2	9 mm^2	1 mm^2	9 mm^2
Fill factor	61%	61%	-	-
Number of microcells	667	3600	400	3600
Peak PDE	35%	35%	33%	33%
DCR	50 kcps	300 kcps	100 kcps	500 kcps
Breakdown voltage	53 V	53 V	95 V	95 V
Structure	p-on-n	p-on-n	p-on-n	p-on-n
Terminal capacitance	60 pF	320 pF	20 pF	175 pF

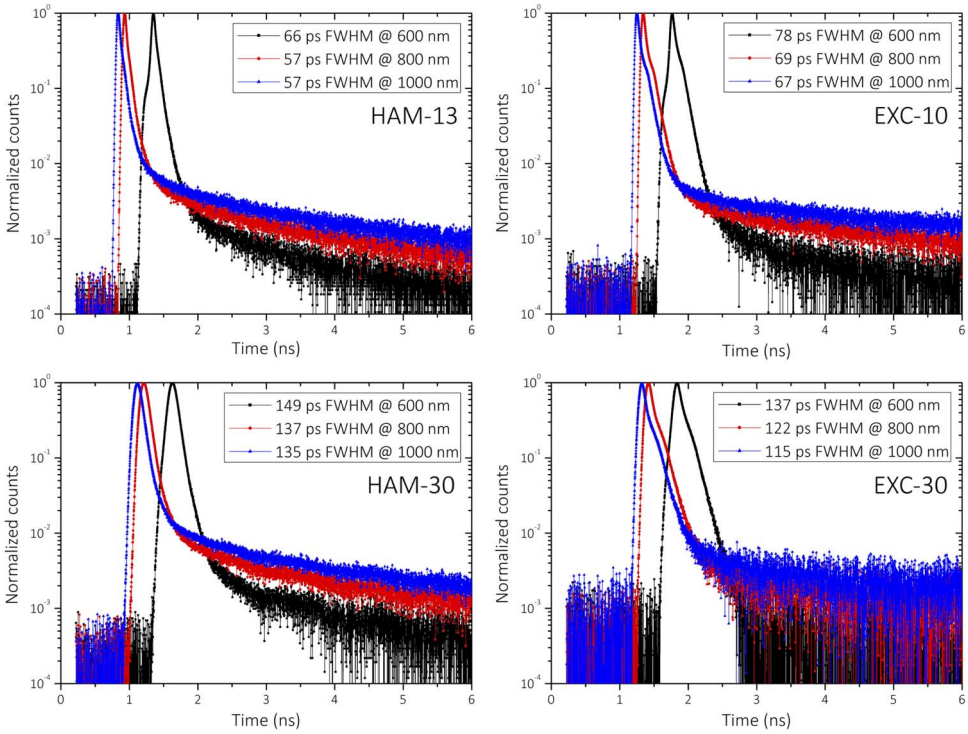

Fig. 3. IRF measured at three wavelengths (i.e., 600 nm, 800 nm, and 1100 nm) for the small area (top) and large area (bottom) SiPMs produced by Hamamatsu (left) and Excelitas (right).

technique is sensitive to "first photon" distortion [31], we kept the photon counting rate always below 5% of the laser pulse rate (i.e., below 2 MHz) to have negligible probability to have more than one photon detection for each laser excitation. The acquired curves were then processed in MATLAB to compute all the parameters of interest, namely noise, SPTR, and decay time constants. The average value of the noise was subtracted from the acquired IRF plot, in order to increase the dynamic range. Then, the FWHM of the curves was computed to obtain the SPTR at every measured wavelength. Fig. 3 shows the IRFs obtained using all SiPM detectors under test,

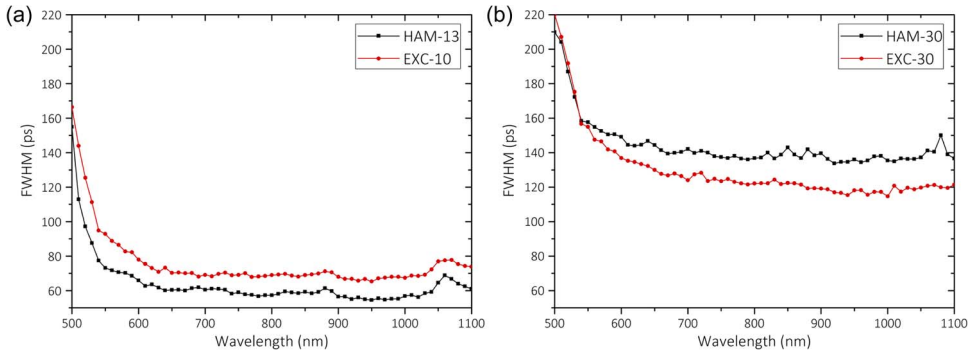

Fig. 4. Single-Photon Time Resolution (SPTR) over the light excitation spectral range for the small (a) and the large (b) area SiPMs.

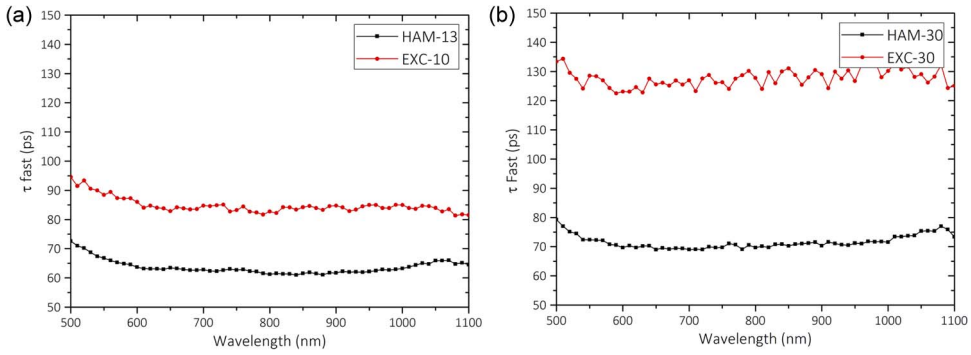

Fig. 5. Measured fast decay time constant over the excitation spectral range for small (a) and large (b) area SiPMs.

at three wavelengths (selected to be well distributed over the spectral range), namely 600 nm, 800 nm, and 1000 nm, in order to show the trend. All reported curves present the previously described typical shape: a fast peak followed by two distinguishable exponentially decaying tails.

4.1. Single-Photon Timing Resolution

Fig. 4 shows the SPTR in terms of FWHM of the detector response peak, over the entire spectral range of light excitation. As it can be seen, the measured timing resolution is almost constant starting from 600 nm up to 1100 nm. The worsening below 600 nm and around 1060 nm is due to the widening of the laser pulse at those wavelengths, as already explained in Section 3.1. It is worth noting that the performance achieved by the HAM-13 SiPM together with our front-end circuitry is 57 ps, which is well below the best result so far reported in literature (i.e., 75 ps [20]), for SiPM detectors of the similar area, thus setting the present world record, to the best of our knowledge. In the same way, the 115 ps jitter measured with the EXC-30 SiPM represents the record in timing resolution for such 9 mm^2 active area samples (up to now limited to 180 ps [23]). This result is in part due to recent improvements in the SiPM fabrication technology and to the optimized electronic front-end.

4.2. Exponential Decays

Fig. 5 shows the fast exponential decay time constant of the SiPMs response. To the best of our knowledge in the literature, there is neither a comprehensive characterization at different wavelengths nor an accepted explanation of this phenomenon affecting the SiPM timing

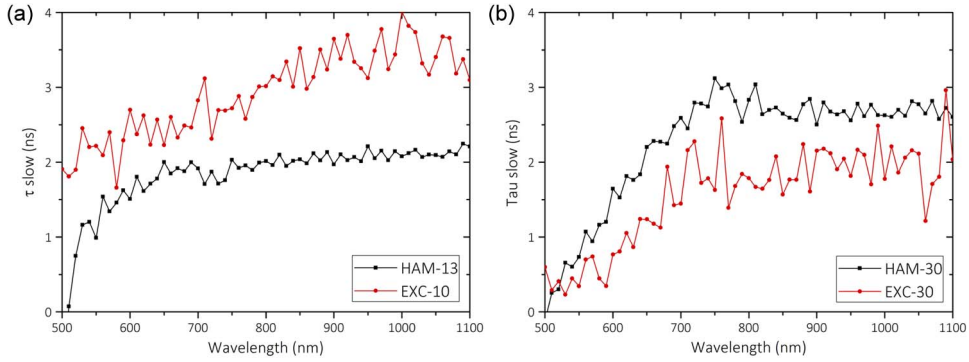

Fig. 6. Measured slow decay time constant over the excitation spectral range, for small (a) and large (b) area SiPMs.

response. From our measurements it is clear that the fast decay of the small area SiPMs is always below 100 ps time constant, which is comparable with the shortest time constant reported for single SPADs. On the other hand, the large area SiPMs feature a time constant always below 150 ps. Additionally, these values are actually constant over the entire light excitation spectra, thus confirming that the IRF response does not depend on the detector behavior but to the electronics; in fact, it is probably due to the high-pass filtering action of the RF amplifier employed in the front-end circuitry, which extracts the (very fast) derivative of the avalanching signal, while leaving a recovery of some hundreds picoseconds, as discussed in Section 3.2. The reported values are extremely advantageous in many TR-DO applications, where the tail could "hide" the true optical properties of homogeneous media or limit the possibility to detect inhomogeneities in turbid samples [13].

Fig. 6 shows the second contribution to the diffusion tail, the slow decaying time constant, which is visible only some (about two) orders of magnitudes below the main peak (as shown in Figs. 1 and 3) and sets also a limit to the detection dynamic range. Additionally, due to its long time constant, such a slow tail limits the maximum exploitable laser repetition rate. As shown, all devices present comparable long decay time constants, and the value is almost constant versus wavelength. The drop at shorter wavelengths is due to the imprecision in computing the time constant, since at short wavelengths photons get progressively absorbed at shorter depths, so the percentage of events contributing to the diffusion tail reduces, thus decreasing the diffusion tail amplitude, though it still keeps the same wavelength independent time constant, as given by (3).

4.3. Dynamic Range

Fig. 7 shows the dynamic range over the light excitation spectrum, computed as described before in Section 2. For all characterized SiPM detectors, the previously described slow exponential decay definitely limits the achievable DR. Furthermore, all characterized detectors experience a reduction of DR at increasing incident wavelength. This is a clear signature of the device-dependent diffusion tail effect, through the W neutral region thickness as shown in (3). Longer wavelength photons are absorbed deeper within the semiconductor, so many of them have to diffuse longer before reaching the depleted space charge region and triggering the avalanche process. Instead at shorter wavelength, the tail intensity (not its time constant) becomes fainter. As can be seen for the HAM-13 SiPM, at 1.5 ns time delay from the main peak, the DR ranges from 800 down to 200 when moving from 500 nm to 1100 nm photon wavelength.

4.4. Dark Count

Eventually we characterized the main noise contributions of the SiPM: the primary DCR and the afterpulsing. Since thermal generation decreases by lowering the temperature, the total

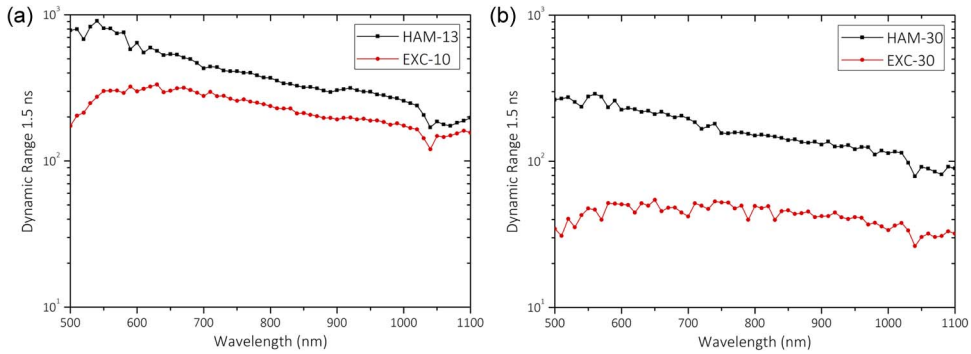

Fig. 7. Measured dynamic range over the excitation spectral range for small (a) and large (b) area SiPMs.

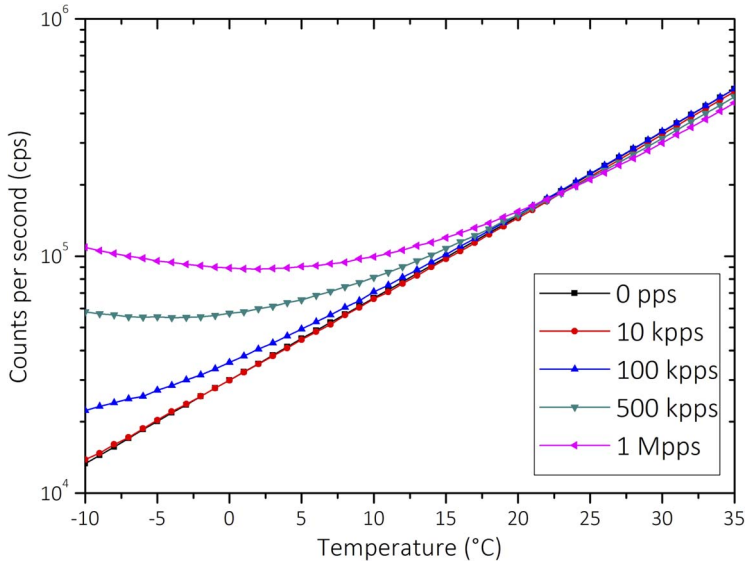

Fig. 8. Measured noise count rate of the EXC-10 device vs. device temperature, at different photon counting rate, from no photon signal (0 photons per second, pps) up to 1 M detected pps.

DCR will correspondingly reduce with temperature. On the other hand, the release time constant of trapped charges increases with decreasing temperature; hence, afterpulsing increases at lower temperatures. Additionally, afterpulsing also depends on the total detection counting rate, since higher number of triggered avalanches will increase the total charge flowing through the device and, consequently, the total probability of having trapped electrons. As showed in Fig. 8 for the EXC-10 device, with no photon signal (i.e., at zero photons per second, pps), the measurement represents the noise floor of the detector, given as counts per second (cps), due to both primary DCR and few afterpulses. In these conditions, afterpulsing is substantially negligible as proved by the pure exponential noise trend vs. increasing temperature, due to the exponential growth of the dark generation rate [16]. Instead the other curves have been acquired by progressively increasing the excitation photon flux, thus highlighting the afterpulsing clear effect at a detected photon rate approaching and then exceeding 100 kpps. The 1 Mpps rate can be considered the upper limit (less than 5%) for avoiding TCSPC pile-up distortions when operating at a laser pulse rate of 40 MHz. As the avalanche rate increases, the number of trapped carriers increases as well, thus bringing to a higher impact of afterpulsing over the total noise of the detector. This measurement allows to quantify the increase of background noise during real

operative conditions and to properly select the best working temperature as a tradeoff between afterpulsing and primary noise at the desired photon counting rate of the specific application of interest (e.g., down to 15 °C at 1 Mpps or down to 0 °C at 100 kpps).

We report such a trend only for one exemplifying detector, namely the EXC-10 SiPM, just to show the general behavior, since we tested that all devices show similar trends. The best operating temperature of course depends on the total photon rate and on the afterpulsing probability for the specific detector under evaluation, and has to be trimmed at the proper value. It is worth noting that 100 kpps is a background count rate that can be highly tolerated in TR-DO, where the maximum count rate set by the pile-up distortion is set at 2 Mcps when using a 40 MHz repetition rate laser.

5. Conclusion

We performed a comprehensive characterization of the response shape of various small (1–1.69 mm^2) and large (9 mm^2) active area SiPM devices produced by two different manufacturers. It is worth noting that we reported results obtained from the best device selected among few samples taken from different manufacturers, but we also experienced a considerable variability of single-photon performance among different production runs. To the best of our knowledge, we reported the world best timing resolution ever achieved, quantified in terms of FWHM as 57 ps for the small SiPM and 115 ps for the large active area one when operated in single-photon regime. This result is due to the design of a custom-made low-noise and wide-bandwidth front-end, able to optimize the avalanche signal pick-up. Additionally, we covered the lack of a comprehensive SiPM response shape characterization in literature, reporting on the spectral behavior of the single-photon response shape, giving information not only about the timing jitter but quantifying the contribution of exponentially decaying tails as well, which is considered crucial for many diffuse optics applications.

Thanks to the obtained results of 57 ps SPTR, lower than 100 kcps DCR at 20 °C, exponential tail time-constant lower than 100 ps, we can conclude that these detectors, that in the past were often discarded for single-photon applications because of their poor temporal resolution and high DCR, are indeed suitable for a vast majority of single-photon applications. SiPMs with front-end similar to the one reported herein can surely replace traditional PMTs in many applications like for example time-resolved diffuse optics, where a large collection area is absolutely required, thus forcing in the past to the use of bulky, fragile and expensive PMT detectors. These systems can now evolve to cheaper, more compact, and reliable instruments, thus paving the way to future widespread deployment of time-resolved diffuse optics systems in many fields. The main limitation of SiPMs is now represented by the slow time constant tail affecting the response, that can hamper the performance in diffuse optics when the optical properties to extract are particularly challenging in case of very high medium absorption). However, this was a problem that affected also the SPAD detectors and was solved by the introduction of novel detector structures, which can be a reference also for next-generation SiPMs.

Acknowledgment

The authors wish to thank Prof. F. Zappa (Dipartimento di Elettronica, Informazione e Bioingegneria—Politecnico di Milano) for useful discussions.

References

[1] B. Dolgoshein *et al.*, "Status report on silicon photomultiplier development and its applications," *Nucl. Instrum. Methods Phys. Res. A, Accel. Spectrom. Detect. Assoc. Equip.*, vol. 563, pp. 368–376, 2006.

[2] D. Renker, "New trends on photodetectors," *Nucl. Instrum. Methods Phys. Res. A, Accel. Spectrom. Detect. Assoc. Equip.*, vol. 571, no. 1/2, pp. 1–6, Feb. 2007.

[3] D. R. Schaart *et al.*, "A novel, SiPM—Array-based, monolithic scintillator detector for PET," *Phys. Med. Biol.*, vol. 54, no. 11, pp. 3501–3512, Jun. 2009.

[4] T. Durduran, R. Choe, W. B. Baker, and A. G. Yodh, "Diffuse optics for tissue monitoring and tomography," *Rep. Progress Phys.*, vol. 73, no. 7, pp. 1–43, Jul. 2010.
[5] A. Dalla Mora *et al.*, "Towards next-generation time-domain diffuse optics for extreme depth penetration and sensitivity," *Biomed. Opt. Exp.*, vol. 6, no. 5, p. 1749–1760, May 2015.
[6] A. Dalla Mora *et al.*, "Fast silicon photomultiplier improves signal harvesting and reduces complexity in time-domain diffuse optics," *Opt. Exp.*, vol. 23, no. 11, pp. 13 937–13 946, Jun. 2015.
[7] A. Torricelli *et al.*, "Time domain functional NIRS imaging for human brain mapping," *Neuroimage*, vol. 85, pp. 28–50, Jan. 2014.
[8] A. T. Eggebrecht *et al.*, "Mapping distributed brain function and networks with diffuse optical tomography," *Nat. Photon.*, vol. 8, no. 6, pp. 448–454, May 2014.
[9] A. Pifferi *et al.*, "Review: Time-domain broadband near infrared spectroscopy of the female breast: A focused review from basic principles to future perspectives," *J. Near Infrared Spectrosc.*, vol. 20, no. 1, pp. 223–235, 2012.
[10] A. Torricelli *et al.*, "Time-resolved reflectance spectroscopy for non-destructive assessment of food quality," *Sens. Instrum. Food Quality Safety*, vol. 2, no. 2, pp. 82–89, Mar. 2008.
[11] A. Farina *et al.*, "Nondestructive optical detection of monomer uptake in wood polymer composites," *Opt. Lett.*, vol. 39, no. 2, pp. 228–231, Jan. 2014.
[12] D. Khoptyar *et al.*, "Broadband photon time-of-flight spectroscopy of pharmaceuticals and highly scattering plastics in the VIS and close NIR spectral ranges," *Opt. Exp.*, vol. 21, no. 18, pp. 20 941–20 953, Sep. 2013.
[13] D. Contini *et al.*, "Effects of time-gated detection in diffuse optical imaging at short source-detector separation," *J. Phys. D. Appl. Phys.*, vol. 48, no. 4, Feb. 2015, Art. ID. 45401.
[14] A. Puszka *et al.*, "Spatial resolution in depth for time-resolved diffuse optical tomography using short source-detector separations," *Biomed. Opt. Exp.*, vol. 6, no. 1, p. 1, Dec. 2014.
[15] M. Mazurenka *et al.*, "Non-contact in vivo diffuse optical imaging using a time-gated scanning system," *Biomed. Opt. Exp.*, vol. 4, no. 4, pp. 2257–2268, Oct. 2013.
[16] F. Zappa, S. Tisa, A. Tosi, and S. Cova, "Principles and features of single-photon avalanche diode arrays," *Sens. Actuators, A Phys.*, vol. 140, no. 1, pp. 103–112, Oct. 2007.
[17] S. Cova, A. Lacaita, and G. Ripamonti, "Trapping phenomena in avalanche photodiodes on nanosecond scale," *IEEE Electron Device Lett.*, vol. 12, no. 12, pp. 685–687, Dec. 1991.
[18] H. Wabnitz *et al.*, "Performance assessment of time-domain optical brain imagers, Part 2: nEUROPt protocol," *J. Biomed. Opt.*, vol. 19, no. 8, pp. 1–12, Aug. 2014.
[19] M. Assanelli, A. Ingargiola, I. Rech, A. Gulinatti, and M. Ghioni, "Photon-timing jitter dependence on injection position in single-photon avalanche diodes," *IEEE J. Quant. Electron.*, vol. 47, no. 2, pp. 151–159, Feb. 2011.
[20] F. Acerbi, A. Ferri, A. Gola, N. Zorzi, and C. Piemonte, "Analysis of single-photon time resolution of FBK silicon photomultipliers," *Nucl. Instrum. Methods Phys. Res. A, Accel. Spectrom. Detect. Assoc. Equip.*, vol. 787, pp. 34–37, Jul. 2015.
[21] A. Gola, C. Piemonte, and A. Tarolli, "Analog circuit for timing measurements with large area SiPMs coupled to LYSO crystals," *IEEE Trans. Nucl. Sci.*, vol. 60, no. 2, pp. 1296–1302, Apr. 2013.
[22] D. Gedcke and W. McDonald, "A constant fraction of pulse height trigger for optimum time resolution," *Nucl. Instrum. Methods*, vol. 55, pp. 377–380, Jan. 1967.
[23] F. Acerbi *et al.*, "Characterization of single-photon time resolution: From single SPAD to silicon photomultiplier," *IEEE Trans. Nucl. Sci.*, vol. 61, no. 5, pp. 2678–2686, Oct. 2014.
[24] V. Puill *et al.*, "Single photoelectron timing resolution of SiPM as a function of the bias voltage, the wavelength and the temperature," *Nucl. Instrum. Methods Phys. Res. A, Accel. Spectrom. Detect. Assoc. Equip.*, vol. 695, pp. 354–358, Dec. 2012.
[25] M. Mazzillo *et al.*, "Timing performances of large area silicon photomultipliers fabricated at STMicroelectronics," *IEEE Trans. Nucl. Sci.*, vol. 57, no. 4, pp. 2273–2279, Aug. 2010.
[26] M. Ghioni, A. Gulinatti, I. Rech, F. Zappa, and S. Cova, "Progress in silicon single-photon avalanche diodes," *IEEE J. Sel. Topics Quant. Electron.*, vol. 13, no. 4, pp. 852–862, Jul./Aug. 2007.
[27] A. Lacaita, M. Ghioni, and S. Cova, "Double epitaxy improves single-photon avalanche diode performance," *Electron. Lett.*, vol. 25, no. 13, pp. 841 843, Jun. 1989.
[28] M. Ghioni, S. Cova, A. Lacaita, and G. Ripamonti, "New silicon epitaxial avalanche diode for single-photon timing at room temperature," *Electron. Lett.*, vol. 24, no. 24, pp. 1476–1477, Nov. 1988.
[29] F. Acerbi *et al.*, "High detection efficiency and time resolution integrated-passive-quenched single-photon avalanche diodes," *IEEE J. Sel. Topics Quantum Electron.*, vol. 20, no. 6, pp. 268–275, Nov. 2014.
[30] I. Bargigia *et al.*, "Time-resolved diffuse optical spectroscopy up to 1700 nm by means of a time-gated InGaAs/InP single-photon avalanche diode," *Appl. Spectrosc.*, vol. 66, no. 8, pp. 944–950, Aug. 2012.
[31] M. Patting, M. Wahl, P. Kapusta, and R. Erdmann, "Dead-time effects in TCSPC data analysis," in *Proc. SPIE*, 2007, pp. 658 307–658 310. [Online]. Available: http://dx.doi.org/10.1117/12.722804